Electronic structure and electron energy-loss spectroscopy of ZrO_2 zirconia

L. K. Dash,[1,*] Nathalie Vast,[1,†] Philippe Baranek,[1,‡] Marie-Claude Cheynet,[2] and Lucia Reining[1]
[1]*Laboratoire des Solides Irradiés, CEA-CNRS UMR 7642 Ecole Polytechnique, 91128 Palaiseau Cedex, France*
[2]*LTPCM/ENSEEG/CNRS, 38402 Saint-Martin d'Hères, France*
(Received 25 June 2004; published 20 December 2004)

The atomic and electronic structures of zirconia are calculated within density functional theory, and their evolution is analyzed as the crystal-field symmetry changes from tetrahedral [cubic (c-ZrO_2) and tetragonal (t-ZrO_2) phases] to octahedral (hypothetical rutile ZrO_2), to a mixing of these symmetries (monoclinic phase, m-ZrO_2). We find that the theoretical bulk modulus in c-ZrO_2 is 30% larger than the experimental value, showing that the introduction of yttria in zirconia has a significant effect. Electronic structure fingerprints which characterize each phase from their electronic spectra are identified. We have carried out electron energy-loss spectroscopy experiments at low momentum transfer and compared these results to the theoretical spectra calculated within the random phase approximation. We show a dependence of the valence and $4p$ ($N_{2,3}$ edge) plasmons on the crystal structure, the dependence of the latter being brought into the spectra by local-field effects. Last, we attribute low energy excitations observed in EELS of m-ZrO_2 to defect states 2 eV above the top of the intrinsic valence band, and the EELS fundamental band gap value is reconciled with the 5.2 or 5.8 eV gaps determined by vacuum ultraviolet spectroscopy.

DOI: 10.1103/PhysRevB.70.245116 PACS number(s): 71.45.Gm, 79.20.Uv, 71.15.Mb, 72.80.Ga

I. INTRODUCTION

Zirconia (ZrO_2) is a technologically important material due to its high strength and stability at high temperatures and its excellent dielectric properties, with an average static dielectric constant ε_0 of around 20.[1] Zirconia thus has a wide range of industrial applications, including uses in ceramic engineering (for example, to strengthen SiC ceramics[2]), as an oxygen sensor in fuel cells,[3] and is also a technologically important catalytic support medium.[4] It is now proposed, together with hafnia, as a gate dielectric material in metal-oxide semiconductor devices.[5,6]

Moreover, zirconia is one of the most radiation-resistant ceramics currently known,[7,8] and therefore has a particular importance in the nuclear industry, where it is used as a passivating medium for hydrogen ingress in pressure tubes. A proposed application of particular interest is the use of a ZrO_2 matrix which can be doped with radioactive nuclei (particularly actinides), and irradiated to force a transmutation process and form nonradioactive dopants in the irradiated and yet stable zirconia matrix.

The evolution of the structural and electronic properties of zirconia as a function of factors such as temperature and pressure in the polymorphs of pure zirconia (cubic, tetragonal or monoclinic phases), as well as their mixing with various oxides is therefore the subject of intensive experimental studies. As for theoretical studies, the structural properties and electronic ground state have been examined, using Hartree-Fock[9,10] or density functional theory (DFT).[11–18] The lattice dynamics of the pure phases have been investigated within density functional perturbation theory[1,19] and the phase stability has been investigated within Landau theory[20,21] or lattice dynamical models[22–24] and reproduced with atomistic or tight-binding models.[25,26] The stabilization of the phases by doping has been investigated both at the Hartree-Fock[27] and DFT[28–32] levels.

Meanwhile, electron energy-loss spectroscopy (EELS) is a useful method for providing information about the chemical and crystallographic environment of a sample, as well as its electronic structure. However, the main drawback of this technique remains the interpretation of the obtained spectra, and therefore theoretical studies are of great use. In calculations of excitations from core levels, dipole matrix elements are generally neglected and the experimental spectra are directly compared to the theoretical density of empty states, projected onto the appropriate atomic state to satisfy the selection rule. The combination of theoretical and experimental techniques applied to core level spectroscopy has already enabled the solution of complex problems such as the nature of bonding in metals and alloys,[33] or the local environments at interfaces.[34,35] Core level spectroscopy has also been applied to zirconia[36,37] to characterize and localize the yttria in the structure.

However, the theoretical interpretation of low-loss (valence) electron energy-loss spectra requires an additional level of complexity in the theoretical framework: using density functional theory as a starting point, one needs to calculate the response function of the material at the level of the random phase approximation (RPA) or beyond, in the quasiparticle picture or further, including the full excitonic effects.[38,39] Application of these methods to semiconductors,[40,41] semimetals,[42] nanotubes[43] or metals[44] has recently demonstrated the usefulness of these techniques to accurately predict valence electron energy-loss spectra.

Despite the technological interest in zirconia, there have been remarkably few experimental studies of EELS in pure[45,46] and doped zirconia.[47,48] In particular, experiments at low transferred momentum have not yet been performed. An *ab initio* calculation of EELS spectra would permit us to make a direct link between the experimental EELS spectra and the electronic structure of zirconia. To our knowledge, this study represents the first *ab initio* determination of the EELS in ZrO_2.

In order to achieve this, after presenting our theoretical framework in Sec. II, we present new results for the atomic (Sec. III) and electronic structure (Sec. IV) properties of the zirconia polymorphs, placed in the context of an analysis of the existing literature (currently very dispersed), which enables us to draw new conclusions for the appropriate treatment of semicore states (Sec. III C) and for the characteristics of the bulk modulus in each phase (Sec. III D). In Sec. IV, we describe the fingerprints of the electronic structure that characterize each phase, and calculate the band structure and fundamental gap for each phase (Secs. IV C–IV E). This is complemented by new experimental EELS results which are described in Sec. V, together with our *ab initio* calculations of the EELS spectra.

II. THEORETICAL METHODS

We use density functional techniques within the plane-wave pseudopotential approach, using the local density approximation for the ground state calculations.[49,50] We use Bachelet, Hamann, and Schlüter type pseudopotentials[51] which, for the zirconium pseudopotential, include the semicore 4*s* and 4*p* states. For these pseudopotentials, we achieve full convergence of the total energy and of the Kohn-Sham eigenvalues at a plane-wave cutoff of 170 Ry. This level of accuracy for the Kohn-Sham eigenvalues and eigenvectors is required to calculate the response function of Eq. (3).

Both a hydrostatic stress tensor and fully relaxed ionic positions were achieved in the calculation of the equation of state of the cubic, tetragonal, and rutile phases. For *m*-ZrO_2, we have relaxed the ionic positions and kept the ratios and angle of the cell parameters at their equilibrium value. The determination of the lattice parameters and bulk moduli has been performed with a $4\times4\times4$ Monkhorst and Pack *k*-point mesh,[52] whereas the band structure calculations were performed with a minimum of 20 *k*-points in each symmetry direction. The convention adopted for high symmetry points is that given in Ref. 53. In order to determine the character of the wave function at the Γ point [Figs. 4(c), 6(c), and 77] we have calculated the character of the representation based on the Kohn-Sham wave function ψ at Γ as $\langle\psi|O\{R|a\}|\psi\rangle$, where $O\{R|a\}$ is the operator associated with the rotation R and the fractionary translation of vector a of the crystal space group.[54]

We then use the Kohn-Sham band structure as a starting point for calculations of the linear dielectric response. Working in reciprocal space, the microscopic dielectric function[55–57] $\varepsilon(\mathbf{r},\mathbf{r}',\omega)$ can be expressed in matrix form in terms of reciprocal lattice vectors $\mathbf{G}$ and a momentum transfer wave vector $\mathbf{q}$ from the first Brillouin zone as $\varepsilon_{\mathbf{GG}'}(\mathbf{q},\omega)$. The loss function, directly related to the EELS spectrum, is then given in terms of the dielectric function as

$$-\mathrm{Im}[\varepsilon^{-1}_{\mathbf{GG}'}(\mathbf{q},\omega)] = -\mathrm{Im}[1+v(\mathbf{q}+\mathbf{G})\chi_{\mathbf{GG}'}(\mathbf{q},\omega)], \quad (1)$$

where v is the Coulomb potential and χ the polarizability of the system. The absorption spectrum is given by the imaginary part of the macroscopic dielectric function, defined as

$$\varepsilon_M(\omega) = \varepsilon_1 + i\varepsilon_2 = \lim_{\mathbf{q}\to\mathbf{0}} \frac{1}{\varepsilon^{-1}_{\mathbf{G}=\mathbf{0}\mathbf{G}'=\mathbf{0}}(\mathbf{q},\omega)}. \quad (2)$$

We can write the polarizability for independent particles (χ_0) in linear response theory as a sum over independent transitions between (Kohn-Sham) states with wave function $\psi_{i,j}$ and transition energies ω_{ij} being the difference between the Kohn-Sham eigenvalues for states ψ_i and ψ_j,

$$\chi_0(\mathbf{r},\mathbf{r}',\omega) = \sum_{i,j}(f_i - f_j)\frac{\psi_i(\mathbf{r})\psi_j^*(\mathbf{r})\psi_j(\mathbf{r}')\psi_i^*(\mathbf{r}')}{\omega-\omega_{ij}+i\eta}, \quad (3)$$

where the $f_{i,j}$ are the occupation numbers. The full polarizability, within the time-dependent density functional theory (TDDFT) approach, is then given by a Dyson-type equation,[58,59]

$$\chi = \chi_0 + \chi_0(v+f_{xc})\chi. \quad (4)$$

Here the exchange and correlation kernel f_{xc}, representing the functional derivative with respect to density of the exchange-correlation potential, is set to zero in our calculations, thus giving us the random phase approximation.

Crystal local-field effects are contained within the Coulomb potential term v, which is the functional derivative of the Hartree potential with respect to density. If we include only the long range part of the Coulomb potential, $v_{\mathbf{G}=0}(q)$, then the microscopic response of the system to the external macroscopic field—the local-field effects—is neglected, and we only need to calculate the head of the dielectric matrix, ε_{00}. If however we include the $\mathbf{G}\neq0$ terms then $\varepsilon_{\mathbf{GG}'}$ is, moreover, not diagonal, and so the matrix inversion has the effect of mixing the previously independent transitions. This can have a large effect on the EELS spectra of the system, particularly with regard to the semicore plasmon peak positions.[40,60] In order to examine this in detail, therefore, in this work we calculate EELS spectra both with and without local-field effects (Sec. V A).

III. ATOMIC STRUCTURE

In this section, we first review the phase diagram and atomic structures of the low pressure phases of zirconia (Secs. III A and III B). In Sec. III C, we then validate the approximations made in our calculations, such as the use of the local density approximation, by comparing our theoretical results to those already in the literature. We will show (Sec. III A) that it is necessary to include zirconium semicore states in the pseudopotential in order to simultaneously describe all the low-temperature phases. Finally, we have calculated the equation of state and bulk modulus of each phase (Sec. III D).

A. Phase stability

Zirconium dioxide is the only thermodynamically stable compound in the system Zr-O.[61,62] At low pressures, zirconia displays three phases: monoclinic, tetragonal, and cubic. At higher pressures, there are further stable phases

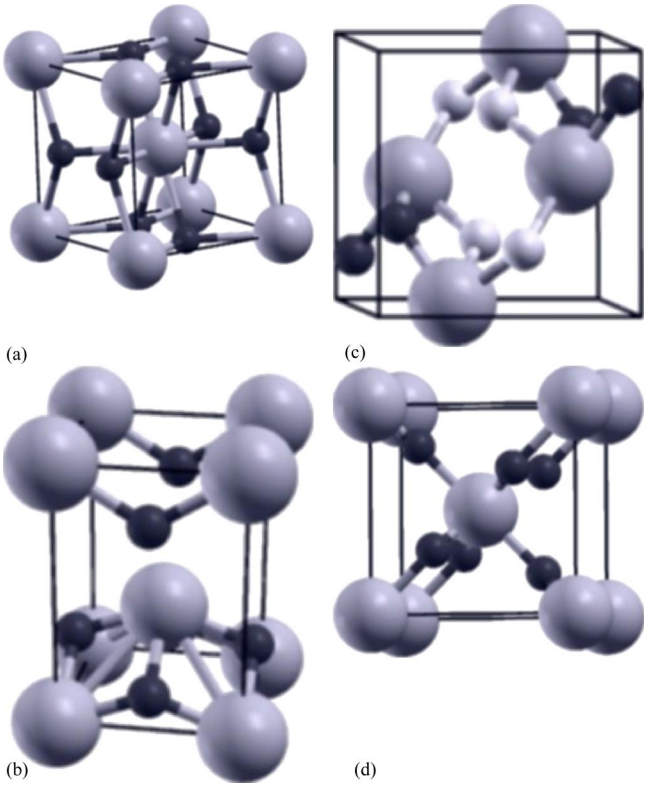

FIG. 1. The primitive unit cell of four atomic structures of zirconia: (a) cubic ZrO_2, (b) tetragonal ZrO_2, (c) monoclinic ZrO_2, (d) zirconia in the hypothetical rutile phase. Large sphere, zirconium atom. Small sphere, oxygen atom. For the monoclinic phase, the two different oxygen sites are shown in different shades.

which we will not consider in this paper (see, for example, Refs. 63–66).

The ground state phase of zirconia, a baddeleyite structure with a monoclinic unit cell, is stable up to around 1480 K.[67] The monoclinic unit cell has nine internal degrees of freedom, and contains four ZrO_2 units [m-ZrO_2, space group $P2_1/c$, $N=4$, Fig. 1(c)].[68]

At 1480 K, monoclinic zirconia (m-ZrO_2) undergoes a first-order martensitic transition to transform into a tetragonal phase[69] [t-ZrO_2, space group $P4_2/nmc$, $N=2$, Fig. 1(b)]. This transformation exhibits a large hysteresis with the $t \rightarrow m$ transition completing at around 1200 K.[70–72] By increasing the temperature to 2650 K, a displacive transition takes place in t-ZrO_2 and the cubic fluorite phase [c-ZrO_2, space group $Fm3m$, $N=1$, Fig. 1(a)][73] is obtained,[67] which is then stable up to the melting temperature of 2983 K.[61]

Nanoparticles of the tetragonal phase are also stable at ambient conditions with grain sizes between 2 and 70 nm.[74] Alternatively, both tetragonal and cubic zirconia can stabilize at ambient temperature by mixing with oxides such as Y_2O_3, MgO or CaO.[75] This introduction of divalent or trivalent cations is accompanied by a structural disorder which can be observed in the Raman spectrum.[76] In this work, we perform calculations on pure zirconia, and the comparison with experimental data allows us to draw some conclusion on the effect of insertion of yttria into zirconia.

B. Phase structure and symmetry

The cubic phase of ZrO_2 has a fluorite structure, which consists of a fcc lattice of zirconium atoms eightfold coordinated to the neighboring oxygen atoms [Fig. 1(a)]. The zirconium site has the octahedral O_h symmetry, while the oxygen atoms are tetrahedrally coordinated to the zirconium atoms.

The tetragonal phase can be obtained from c-ZrO_2 conceptually by expanding the cubic cell in one direction and slightly displacing the oxygen atoms along the tetragonal axis, the coordination around a zirconium atom remaining eightfold [Fig. 1(b)]. The symmetry of the zirconium site is thus lowered to D_{2d} symmetry.

The atomic arrangement in the baddeleyite can also be obtained by a distortion of the simple fluorite structure: the coordination of the zirconium atoms is $Z=7$, and is formed by two nonequivalent oxygen sites [Fig. 1(c)]. One-half of the oxygen atoms are tetrahedrally coordinated as in the fluorite phase, the other one-half have a $Z=3$ coordination, as in the rutile phase. The zirconium and oxygen sites have the same low C_1 symmetry.

The coordination of the zirconium atom is reduced to $Z=6$ in the hypothetical rutile structure [r-ZrO_2, space group $P4_2/mnm$, $N=2$, Fig. 1(d)]. The oxygen atoms form a tetragonally distorted octahedron around the zirconium atoms. The zirconium site has the T_h-related D_{2h} symmetry.

The different phases of zirconia thus allow us to explore the change of the crystal-field symmetry from octahedral-like in the cubic or tetragonal phase to tetrahedral-like in the (hypothetical) rutile phase, via the partially octahedral and partially tetrahedral crystal field in monoclinic zirconia. We use the rutile phase as a tool to investigate effects of the crystal field in zirconia and better understand the properties of the complex monoclinic phase of zirconia.

C. Theoretical structure and phase stability

Rutile is the thermodynamically stable phase of TiO_2. The titanium atom has a $3d^24s^2$ electronic configuration, analogous to the $4d^25s^2$ configuration of the Zr atom. For the rutile phase of ZrO_2, we find the internal parameter, relative to the oxygen position, is $u_O=0.3055$ (as in TiO_2) (Table I). However, a relative energy as high as 0.3 eV/ZrO_2 unit and a volume expanded by 10% with respect to the monoclinic phase (Table I) excludes rutile as a possible phase of zirconia.

The calculated cell parameters at the theoretical equilibrium for the monoclinic, tetragonal, and cubic phases of zirconia are reported in Table I. These values agree extremely well (to within 1%) with experimental values obtained by neutron diffraction[70,73,77] performed on the three phases, and are similar to those reported by previous theoretical calculations which include the $4s^24p^6$ semicore electrons as valence states.[1,13,14,28]

Internal degrees of freedom for the monoclinic phase are also very close to the experimental ones measured by x-ray[68] or neutron diffraction.[77] The error between these two experimental techniques is as large as the error between our *ab initio* value and the value measured by x-ray diffraction.[68]

TABLE I. Structural parameters of *c*-, *t*-, *m*-, and *r*-ZrO_2, and their relative energies (eV/ZrO_2 unit). Experimental structural data for *c*- and *t*-ZrO_2 have been linearly extrapolated to 0 K. Experimental relative energies are the enthalpy differences measured at the temperature of the phase transition. Our results are compared with previous LDA-pseudopotential calculations that include the Zr 4*sp* semicore shells [GW (Ref. 13), US (Ref. 1), and PP (Ref. 28)], with LDA linear augmented plane-wave calculations including semicore states in the valence [FLAPW (Ref. 14)], and with GGA-pseudopotential results that implicitly include the Zr 4*sp* semicore shells via the NLCC (Ref. 29) (US-GGA), or including only the 4*p* (Ref. 15) (4*p* US-GGA).

		This work	GW	US	PP	FLAPW	Expt.	Expt.	US-GGA	4*p* US-GGA
Cubic	a (a.u.)	9.518	9.514	9.5187	9.596	9.551	9.619[a]		9.619	9.768
Tetragonal	a (a.u.)	6.736	6.734	6.7211	6.792	6.747	6.76[a]	6.79[b]	6.856	6.913
	c/a	1.438	1.432	1.434	1.438	1.425	1.453[a]	1.445[b]	1.447	1.468
	d_{z_O}	0.0441	0.0423	0.0418	0.0440	0.0290	0.051[a]	0.050[b]	0.049	0.061
	E_t-E_c	−0.049	−0.045	−0.044	−0.048		−0.057[e]		−0.07	−0.08
Monoclinic	a (a.u.)	9.642	9.611	9.653	9.733		9.733[c]	9.723[d]	9.811	9.906
	b (a.u.)	9.790	9.841	9.769	9.885		9.849[c]	9.841[d]	9.949	10.025
	c (a.u.)	9.947	9.876	9.962	9.961		10.048[c]	10.036[d]	10.125	10.223
	β (deg)	99.65	99.21	99.21	99.23		99.23[c]	99.23[d]	99.81	99.23
	x_{Zr}	0.2776	0.2779	0.2769	0.2769		0.2754[c]	0.2758[d]	0.277	0.2765
	y_{Zr}	0.0427	0.0418	0.0422	0.0430		0.0395[c]	0.0411[d]	0.044	0.0421
	z_{Zr}	0.2092	0.2099	0.2097	0.2100		0.2083[c]	0.2082[d]	0.209	0.209
	x_{O_I}	0.0704	0.0766	0.0689	0.0640		0.0700[c]	0.0703[d]	0.072	0.071
	y_{O_I}	0.3372	0.3488	0.3333	0.3237		0.3317[c]	0.3359[d]	0.338	0.337
	z_{O_I}	0.3407	0.3311	0.3445	0.3524		0.3447[c]	0.3406[d]	0.341	0.342
	$x_{O_{II}}$	0.4482	0.4471	0.4495	0.4497		0.4496[c]	0.4423[d]	0.447	0.450
	$y_{O_{II}}$	0.7576	0.7588	0.7573	0.7560		0.7569[c]	0.7549[d]	0.758	0.758
	$z_{O_{II}}$	0.4807	0.4830	0.4798	0.4790		0.4792[c]	0.4781[d]	0.479	0.479
	E_m-E_t	−0.064	−0.05(7)	−0.04(5)	−0.06(3)		−0.061[e]		−0.10	−0.11
Rutile	a (a.u.)	9.116								
	c/a	0.668								
	u_O	0.3055								
	E_r-E_m	+0.266								

[a] $t\rightarrow c$ transition, neutron diffraction [Aldebert *et al.* (Ref. 73)].
[b] $t\rightarrow m$ transition, neutron diffraction [Frey *et al.* (Ref. 70)].
[c] Neutron diffraction [Howard *et al.* (Ref. 77)].
[d] X-ray diffraction [Smith *et al.* (Ref. 68)].
[e] At the transition temperature [Ackermann *et al.* (Ref. 67)].

The largest error is found on the *y* coordinate of the zirconium atom and amounts to 1.6×10^{-3}, +4% (respectively, 3.2×10^{-3}, +8%) with respect to the x-ray[68] (respectively, neutron[77]) data. The internal degree of freedom of the tetragonal phase, relative to the position of oxygen along the tetragonal axis, shows a dependence both on the temperature and on the direction of the transition $t\rightarrow m$ or $m\rightarrow t$.[70] This can explain the discrepancy with the theoretical values (−13%), an explanation that has previously been reported.[1,14,83]

Several levels of approximation have been used in previous calculations for zirconia. When the Zr 4*sp* semicore states are included neither explicitly nor implicitly [via a nonlinear core correction[84] (NLCC)], and the LDA is used, Christensen and Carter[83] report good agreement, both with experiment and fully linearized augmented plane-wave (FLAPW) calculations,[14] for the structural parameters of *c*, *t*, and *m* zirconia. When both the NLCC and the generalized gradient approximation (GGA) are used, as in the work of Foster *et al.*,[29] structural parameters are also very close to experiment and are systematically slightly larger than experimental data, as expected (Table I). Including the $4p^6$ semicore states, and not the $4s^2$ electrons, but using a "partial core correction" in the solid state, as in the work of Jomard *et al.*,[15] leads to larger errors on all structural quantities of the cubic and tetragonal phases, the densest ones (Table I). This can be understood from the large spatial overlap between the 4*s* and 4*p* states, leading to a large exchange interaction, which is partially neglected in the pseudopotential used in these calculations.

The validity of our approximations (the explicit inclusion of the Zr 4*sp* states and the LDA) has been checked in a previous work by the examination of the calculated equilibrium bond length of the Zr-O molecule.[28] Moreover, we have examined the relative energies of the monoclinic, tetragonal, and cubic phases as in Ref. 27 (Table I). Our results are close to those of a full-potential linear muffin-tin orbital (FP-LMTO) calculation,[26] $E_t-E_c=0.049$ eV and $E_m-E_t=0.056$ eV, in which the Zr 4*s* are treated in a frozen overlapping core approximation. There is also extremely good agreement between our results and values from experiment,[67] obtained as the enthalpy differences between two phases at

the transition temperature: the discrepancy with experiment reaches 14% for $E_t - E_c$, and 0.5% for $E_m - E_t$. The LDA calculation excluding 4*sp* states (Ref. 83, not included in Table I) shows somewhat larger but still reasonable discrepancy with experiment (20% for both $E_t - E_c$ and $E_m - E_t$). Neglecting the semicore states has little effect on the relative properties of the distorted fluorite phases, but it is likely that this will not be the case for widely differing structures. In contrast, the GGA/NLCC calculation (Foster *et al.*[29]) systematically overestimates the absolute value of the energy differences, by 22% for the quantity $E_t - E_c$ (13 meV per ZrO_2 unit), and by more than 50% for $E_m - E_t$ (equivalent to a difference in an activation temperature of 453 K), even though the structural parameters are in close agreement with experiment, as seen above.

This would lead us to conclude that the Zr semicore states are important for the ground state of zirconia. The 4*p* semicore states appear to be sensitive to the environment of the solid, as we will show in Sec. IV A. Therefore, due to the strong spatial overlap with the valence states, the core-valence exchange energy changes in the solid, and it becomes necessary to include these electrons as valence states in the solid calculations. Moreover, the exchange interaction between the 4*s* and 4*p* states must be taken into account. The good agreement between our calculations and experimental data allows us to now make a detailed comparison of the parameters of the equation of state obtained in our calculations and in the experiments.

D. Equation of state and bulk modulus

The equilibrium volume, bulk modulus and its pressure derivative were deduced from a fit of the total energy curve as a function of volume with the Murnaghan equation of state,[85] and are reported in Table II for the monoclinic, tetragonal, cubic, and rutile phases. Our equilibrium volumes are 2% smaller than a previous calculation performed with a smaller plane-wave basis,[28] and 3% smaller than the experimental data. The calculated volume changes of −5% (−1.7 Å^3 per ZrO_2 unit) ($V_0^m \leftrightarrow V_0^t$) and −2% (−0.62 Å^3 per ZrO_2 unit) ($V_0^t \leftrightarrow V_0^c$) are somewhat larger than the volume changes observed at the transition temperature, −3.2% ($V_0^m \rightarrow V_0^t$) (Ref. 71) and −1.2% ($V_0^t \rightarrow V_0^c$).[73]

The theoretical bulk modulus for the monoclinic phase agrees relatively well (difference of +5%) with the value of 189 GPa, estimated from the elastic constants

$$B_V = \tfrac{1}{9}(C_{11} + C_{22} + C_{33}) + \tfrac{2}{9}(C_{12} + C_{23} + C_{13}), \qquad (5)$$

in which the experimental elastic constants[81] are used. Equation (5) is the Voigt approximation, based on the assumption that the strain is uniform everywhere in the sample, and gives an upper limit B_V to the crystal bulk modulus B_0.[86] The smaller value of the bulk modulus measured in Ref. 82 would indicate that in the diamond anvil cell the pressure may have been somewhat higher than the measured pressure, as can be deduced from the small value of the equilibrium volume reported in that particular experiment[82] with respect to other experimental techniques[68,77] (Table II).

TABLE II. Theoretical equations of state of *c*-, *t*-, *m*-, and *r*-ZrO_2 from a fit of the total energy curve with the Murnaghan equation. Plane-wave pseudopotential (PP) results are from Stapper *et al.* (Ref. 28).

		V_0 (Å^3/ZrO_2)	B_0 (GPa)	B_0'
Cubic	This work	31.94	269	4.0
	PP	32.73	268	3.6
	Expt.	32.97[a]	194[b]–209[c]	
Tetragonal	This work	32.56	207	5.0
	PP	33.39	197	5.0
	Expt.	33.28[a], 33.47[d]	190[e]	
Monoclinic	This work	34.26	199	2.6
	PP	35.04	185	1.8
	Expt.	35.06[f], 35.22[g]	189[h]	
	Expt.[i]	34.0	95[i]	4–5[i]
Rutile	This work	37.51	216	4.4

[a] $t \rightarrow c$ transition (Ref. 73), volume extrapolated to 0 K.
[b] Pure ZrO_2 extrapolated from YS ZrO_2 (Ref. 78).
[c] Extrapolated from single crystals YS ZrO_2 (Ref. 79).
[d] $t \rightarrow m$ transition (Ref. 70), volume extrapolated to 0 K.
[e] Yttria stabilized zirconia (Ref. 80).
[f] Single crystal x-ray diffraction (Ref. 68).
[g] Powder neutron diffraction (Ref. 77).
[h] Voigt limit, with C_{ij} from Ref. 81.
[i] DAC experiment (Ref. 82).

The theoretical bulk modulus for the tetragonal phase is close to the experimental value, but larger by +9% with respect to the value obtained by the extrapolation at vanishing yttria content of the bulk moduli of yttria-stabilized tetragonal phases.[80] The difference between theory and experiment ranges from +5% in pure *m* zirconia to +9% for (YS) *t*-ZrO_2 which are both within the limits for the usual difference between LDA and experiment.

Turning to the cubic phase, the elastic constants C_{11} and C_{12} have been measured in yttria-stabilized ZrO_2 as a function of yttria concentration; we have extrapolated these linearly to pure *c*-ZrO_2. The upper limit of the bulk modulus $B_V = (C_{11} + 2C_{12})/3$ (Voigt approximation) for the pure phase is found to be either 194 GPa (extrapolated from the experimental values given in Ref. 78, measured in samples containing from 8 to 18 mol% Y_2O_3) or 209 GPa (extrapolated for the pure phase from a different experiment[79] on single crystals containing 1.7 to 20 mol % yttria). Moreover, we note that in this range of concentrations, the change in elastic constants relative to yttria concentration is weak.

Now, our theoretical bulk modulus for the cubic phase, 269 GPa, is higher by 29% to 39% from the experimental value of 194–209 GPa,[79] a difference much larger than for the tetragonal or monoclinic phases (Table II). We find from the comparison with experimental data that the introduction of yttria in zirconia remarkably *decreases* the bulk modulus at ambient temperature with respect to the (hypothetical at this temperature) pure tetragonal or cubic phase. We also find that the bulk modulus should increase by 30% between the tetragonal and the cubic pure phase, in contrast to the small variation found experimentally[79] between the yttria-

stabilized tetragonal and YS cubic phases. This effect cannot be explained solely from the small increase of the lattice parameter in YS c-ZrO_2, e.g., 1% at 12 mol % of Y_2O_3.[87]

Finally, the presence of dopants (particularly yttria) has two effects: it maintains the microstructure of the ceramics by preventing the sequence of phase transitions $m \rightarrow t \rightarrow c$, and it is known to increase the strength, toughness, and thermal-shock resistance of zirconia.[27] Therefore our finding of a larger bulk modulus in the pure cubic phase than in the YS cubic zirconia would seem paradoxical. However, the two pictures can be reconciled under the hypothesis that at a higher temperature, the elastic properties of pure cubic zirconia evolve more dramatically than the elastic properties of YS zirconia. A comparison of the experimental equation of state of pure cubic and YS cubic zirconia at the same temperature would therefore be useful. This would require the stabilization of the cubic phase at moderate temperature, as high-pressure experiments in diamond anvil cells cannot be performed at 2650 K. This stabilization could be achieved by decreasing the size of nanoparticles of zirconia: nanoparticles stabilize the tetragonal phase at ambient conditions. The reduction of the size of the nanoparticles could lead to the stabilization of the cubic phase, at moderate temperature, which has not been achieved so far.

IV. ELECTRONIC STRUCTURE

In this section, we investigate the evolution of the electronic structure in the polymorphs in relation with the evolution of the symmetry of the crystal field. We examine the excitation spectra of the Zr 4*s* and 4*p* states (Sec. IV A), and the line shape of the O 2*s* peak (Sec. IV B). Results from x-ray photoemission experiments are reported in the literature for the pure monoclinic phase and for yttria-stabilized cubic and yttria-stabilized tetragonal phases,[88] which allow us a comparison with the Zr 4*p* semicore states and with the O 2*s* band. We furthermore give a comparison of the theoretical band structure of the valence (Sec. IV C) and conduction bands (Sec. IV D) in the various phases. Last, we report our results for the theoretical gap, and the gap values determined experimentally from our EELS experiments (Sec. IV E).

A. Electronic structure of zirconium 4*s* and 4*p* semicore levels

Figure 2 shows the total density of states (DOS) for the cubic, tetragonal, monoclinic, and rutile phases. From now on, we fix our reference energy at the top of the valence band of each phase, as reported in Sec. IV C (Fig. 4 and in Table III). Throughout this section, the calculated DOS is a sum of Gaussian functions with a 0.01 Ry width. The peak intensities in the DOS have been scaled to one ZrO_2 unit, thus in order to obtain the DOS per unit cell they should be doubled in the tetragonal and rutile phases, and multiplied by four in m-ZrO_2.

We have found little hybridization for the deep 4*s* and 4*p* states. However, we find that the peaks are not aligned in the four polymorphs: the Zr 4*s* and 4*p* peak positions for the cubic phase are found to be at −0.7 eV (lower) with respect

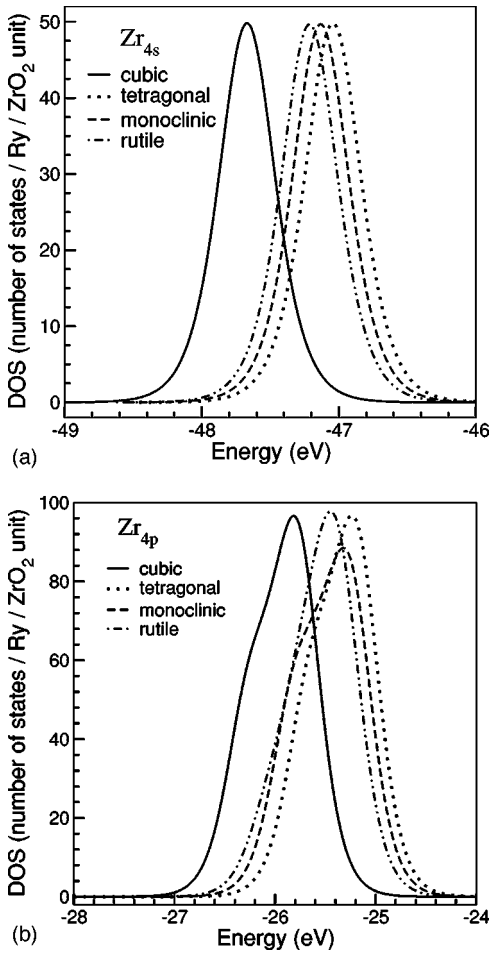

FIG. 2. Density of the Zr 4*s* (a) and 4*p* (b) states in the cubic, tetragonal, monoclinic, and rutile phases. The reference of the energy is the top of the valence band of each phase.

to the tetragonal one (rutile, −0.2 eV, monoclinic, −0.1 eV). These shifts are not observed in the XPS experiment[88] on the Zr 4*p* states because of the arbitrary choice of the reference energy. Indeed, the top of the valence band is not known experimentally: the experimental spectra have been referenced on the top edge of the valence XPS spectra which does not vary between the different phases.[88] As we will show in Sec. IV C, we find in our calculations that the valence DOS are quite similar around the top of the valence band in *c*, *t*, and *m* zirconia [Fig. 5(a)]. However, the calculated valence edge in the tetragonal phase is much sharper than in the cubic or monoclinic phases, as can be deduced from the presence of a higher density of states at the reference energy in t-ZrO_2. This is caused by the contribution of several points in the tetragonal Brillouin zone, generating a higher density of states at the top of the valence band, an observation which is missed when the XPS edges are aligned in this particular experiment.[88]

In our calculations at deep energies, −49 to −46 eV, the effect of the crystal field is small and thus the Zr 4*s* states are atomiclike and the line shape is identical in the four phases, as can be seen from Fig. 2(a). In the −27 to −25 eV energy range [Fig. 2(b)], the Zr 4*p* lines are only 0.3 eV broader than the Zr 4*s* lines, but the calculated line shape is modified

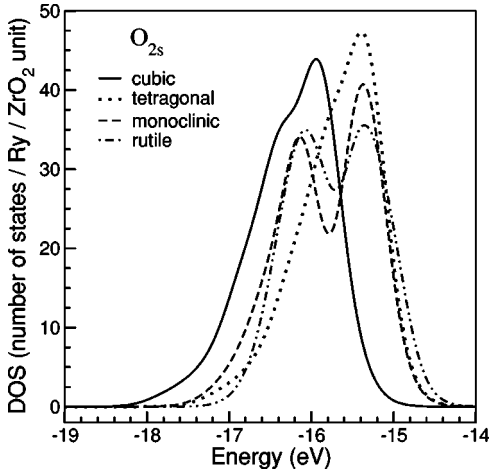

FIG. 3. Density of the O 2*s* states in the cubic, tetragonal, monoclinic, and rutile phases. The reference of the energy is the top of the valence band of each phase.

by the crystal field: it is symmetrical in the rutile phase; in contrast it consists of a double peak separated by 0.5 eV in the three fluorite-derived structures. The peak maximum is found to be 10% less intense in the monoclinic phase with respect to the cubic and tetragonal phases.

To our knowledge, no experimental spectra are available for the Zr 4*s* line. The experimental XPS 4*p* line shapes[88] in the three fluorite-derived structures agree well with our calculations. In particular, it is found both theoretically and experimentally that the shape of the 4*p* doublet is not affected by the change in the coordination shell of zirconium, from $Z=8$ (*c* and *t* zirconia) to $Z=7$ (monoclinic phase). Finally, we compare our theoretical line shapes for the pure phases with those observed in yttria-stabilized *c*- and *t*-ZrO_2,[88] and conclude that the introduction of yttria has no influence on the Zr 4*p* lines, at variance with the findings of Kralik *et al.*[13]

In the monoclinic phase, the experimental Zr 4*p* peaks are at −28.3 eV (main peak) and −29.9 eV (shoulder), a deviation of −3.0 and −4.2 eV, respectively, from our calculated values. By directly comparing our occupied DOS with the XPS spectra, we have neglected the quasiparticle shifts.[38] These have been estimated by Kralik *et al.*[13] and lead to a partial correction of about −1.4 eV in the cubic phase. Another estimate can be provided by an atomic calculation including the self-interaction correction (SIC):[89–91] we found the shift of the SIC to be −6.4 eV for the 4*p* states (−7.1 eV for the 4*s* states) in the zirconium atom, twice the experimental value.

B. Electronic structure of the oxygen 2*s* levels

The O 2*s* DOS curve[93] is reported in Fig. 3 for *c*-, *t*-, *m*-, and *r*-ZrO_2. As was the case for the Zr 4*s* and 4*p* lines, the O 2*s* peak position is lower by −0.5 eV in the cubic phase than in the tetragonal phase (Fig. 3). However, in contrast to the Zr 4*s* and 4*p* lines, the oxygen 2*s* band is very sensitive to the oxygen local coordination.

We find that in the cubic phase, the oxygen atoms are surrounded by four Zr atoms at 2.18 Å. The O 2*s* band shows a left shoulder at −0.5 eV with respect to the main peak.

Second, we see that the oxygen line shape is identical for the cubic and tetragonal structures, in which the O-Zr bond lengths are on average 2.18 Å (2.07 and 2.33 Å in *t*-ZrO_2).

In the rutile structure, the oxygen atoms are surrounded by three Zr atoms at quasiequal distances, 2.087 and 2.084 Å. The O 2*s* band shows two peaks of equal intensity separated by 0.7 eV.

Finally, we can see that for the monoclinic phase, four oxygen atoms have a threefold coordination with the zirconium atoms, at an average distance of 2.04 Å, which is typical of the rutile structure. They contribute to the highest energy O 2*s* peak. Four oxygen atoms have a fourfold coordination with the zirconium neighbors which are at an average distance of 2.18 Å, as in the cubic phase. These atoms contribute to the low energy peak. The mixed coordination shell in *m*-ZrO_2 is then reflected in the DOS (Fig. 3), which shows two peaks separated by 0.7 eV, and a higher intensity at higher energy.

In comparison with the experimental results, we note that experimentally[88] the O 2*s* band is found to be centered at −19 eV in the monoclinic phase. In contrast, we find our O 2*s* doublet located at −16.1 and −15.4 eV. The quasiparticle effects estimated in the cubic phase only partially correct the DFT result, by −2 eV (Ref. 13) and not the −3 eV required to reconcile theory and experiment. Moreover, our LDA bandwidth amounts only to 2 eV. Thus the observed bandwidth of 8 eV (Ref. 88) is explained neither in the LDA nor in the standard application of the quasiparticle framework.[13] Last, we note that despite the error in absolute value on both the Zr 4*p* and O 2*s* peak positions, the theoretical and experimental energy separation between the Zr 4*p* line and the O 2*s* band are similar, within the precision of the experimental data, which is limited by the definition of the band center of the O 2*s* band.[88] This amounts to 9.3 eV experimentally, 9.7 eV in our LDA calculation, and to 9 eV in the GW calculation.[13] This is surprising, as one would expect an LDA error larger on the atomic Zr 4*p* states than on the O 2*s* ones, as the self-interaction potential is expected to be small for extended valence states but not for atomiclike states.[89–91]

C. Electronic structure of the valence band

The dispersion of the energy of the valence bands for the monoclinic, tetragonal, cubic, and rutile phases at the theoretical equilibrium lattice parameters are reported in Fig. 4. The top of the valence band is located at *X* in the cubic phase, and at Γ in *m*- and *r*-ZrO_2. In the tetragonal phase, within the numerical accuracy of our calculation, the top of the valence band is formed by four points located at *A*, at 0.60 $|\Gamma$-$M|$ along the Γ-*M* direction, at 0.63 $|\Gamma$-$X|$ along the Γ-*X* direction, and at *Z*. As already mentioned in Sec. IV A, in the DOS reported for the tetragonal phase in Fig. 5(a) shows a much higher density of states at the top of the valence band (zero energy) with respect to the other phases (regardless of whether experimental or theoretical lattice parameters are used in the calculation)—this is explained by the flat top of the valence band along Γ-*Z*, Γ-*X*, and Γ-*M*,

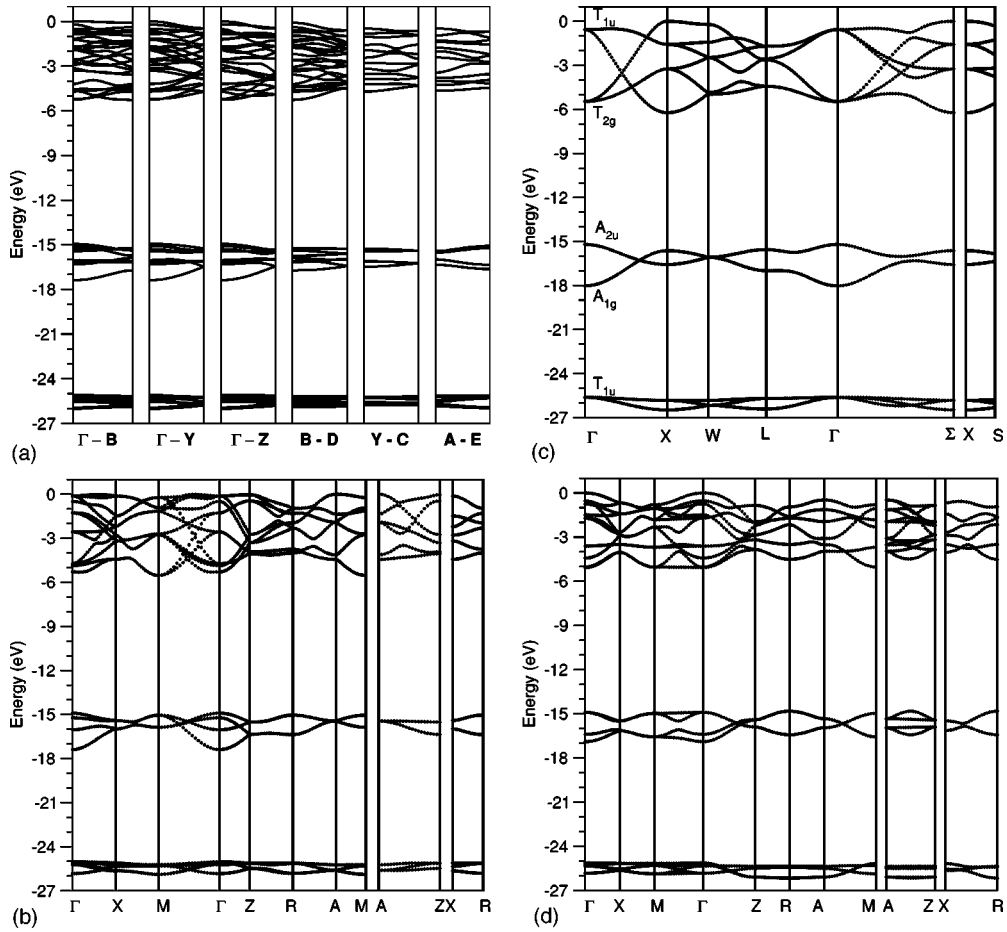

FIG. 4. Theoretical valence band structure at the equilibrium cell parameters for monoclinic (a), tetragonal (b), cubic (c), and rutile (d) zirconia.

which adds to the contributions of the *A* point [Fig. 4(a)].

The valence bandwidth decreases by 1 eV between the tetrahedral and the octahedral crystal fields, from 4.8 eV in the cubic phase (respectively, 4.6 eV in the tetragonal phase) to 3.8 eV in the rutile phase. The valence bandwidth of the monoclinic phase (4.5 eV) is closer to the width of the cubic or tetragonal valence band than to the rutile one.

The agreement between our DOS and the experimental spectrum is excellent [Fig. 5(b)]. The measurement of the photoemission spectrum (from Soriano *et al.*[92]) has been performed at ambient conditions, and therefore probably on the monoclinic phase, as can clearly be seen by comparison with our theoretical DOS. The theoretical spectrum shows a main peak and a shoulder downshifted by −1.5 eV, as in the rutile phase, whereas in the cubic (respectively, tetragonal) phase we see a double peak separated by 2.3 eV (respectively, 2.2 eV). In the experiment, a weak signal not present in the theoretical spectrum is observed at 2 eV above the intrinsic top valence band, and has been attributed to oxygen vacancies on the surface.[92]

D. Electronic structure of the conduction band

The dispersion curves of the conduction bands at the theoretical equilibrium lattice parameters are reported in Fig. 6. The bottom conduction band is found to be at the Γ point in *c*- and *t*-ZrO_2, at the *B* point in the monoclinic phase, and at the *R* point in the rutile phase.

The first conduction bands are found to have an E_g character at Γ in the cubic phase [Fig. 6(c)]. At higher energy, conduction bands have A_{1g} or T_{2g} character at the Γ point. We will show that the separation between the E_g and $A_{1g}+T_{2g}$ bands is a fingerprint of the conduction band in cubic zirconia. The gap in the conduction band has a minimum of 1.4 eV at the *X* point [Fig. 6(c)].

Turning to the empty DOS of *c*-ZrO_2 [Fig. 7(a)], we find that the E_g bands give rise to an intense peak at 4.2 eV, while the T_{2g} band leads to a double structure at 6.7 and 7.9 eV. Although lower in energy at Γ, the free-electron-like A_{1g} state shows a large dispersion and therefore contributes to the DOS only at high energy, between 10 and 13 eV.

On going from a tetrahedral crystal field, as in the fluorite phase, to a (tetragonally distorted) octahedral one in the hypothetical rutile phase, the change is drastic and the relative positions of the E_g and T_{2g} bands are exchanged, as expected from crystal-field theory. In the rutile phase, the T_{2g} derived states now form the lowest conduction bands. A pseudogap opens at 7 eV, where the low DOS consists of the tetragonally distorted A_{1g} band. The E_g derived band now appears at 8 eV.

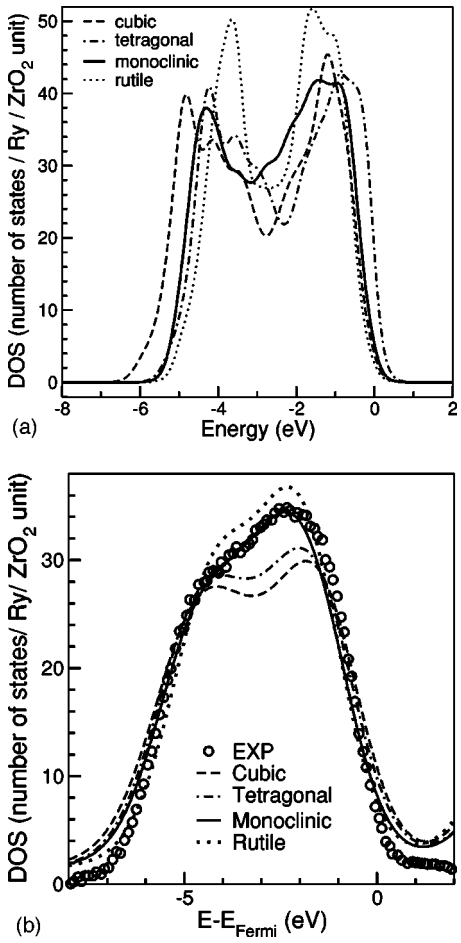

FIG. 5. (a) Theoretical density of the valence states in the cubic, tetragonal, monoclinic, and rutile phases, and (b) its convolution with a Voigt profile consisting, respectively, of a Gaussian function (half-width at half-maximum of 0.8 eV) and of a Lorentzian function (HWHM in eV, $0.2+0.09\times\mathrm{E}$), to be compared to the experimental valence photoemission spectrum (Ref. 92) (arbitrary units).

In contrast, for t-ZrO_2 the tetragonal deformation barely modifies the empty cubic DOS apart from a blueshift: the E_g (respectively, T_{2g} and A_{1g}) band is raised by 0.9 (respectively, 0.6 and 0.4) eV [Fig. 7(a)]. The E_g-A_{1g} separation comes from the $A\rightarrow M$ gap, and these points are both related to the X point of the cubic phase.

In our calculation for the monoclinic phase, the gap in the conduction band separating the bands derived from E_g and T_{2g} cubic bands is lost, a consequence of the partly octahedral and partly tetrahedral crystal field [Fig. 7(a)]. The absence of the gap is confirmed in the experimental Bremsstrahlung isochromat spectrum of Soriano *et al.*[92] [Fig. 7(b)]. The BIS agrees well with our calculated spectrum for m-ZrO_2, convoluted with a Voigt profile, at energies up to 10 eV. At higher energies, a direct comparison is hindered by a significant additional contribution in the experimental spectrum. This is caused by secondary electrons,[94] excited at high energy, whose de-excitation leads to an additional signal at an energy equal to two times the energy gap.[92]

E. Band gap

The fundamental gap of a single crystal of pure zirconia has been measured in the monoclinic phase, on heavily twinned single crystals.[88] More precisely, vacuum ultraviolet spectroscopy has been performed in reflectivity in the 3–40 eV range, and the absorption spectrum has been deduced from a Kramers-Kronig analysis.[88] The band gaps obtained from a fit of the low (respectively, high) absorption is found to be 5.8 (respectively, 7.1) eV.[88] An optical absorption experiment has also been performed on films of monoclinic zirconia between 4.9 and 6.5 eV, and two allowed direct interband transitions were identified at 5.2 and 5.8 eV.[97] However, EELS experiments at large momentum transfer[45,46,95] give a gap value of about 4 eV in the monoclinic phase. How can we explain this discrepancy? In fact in optical experiments, an absorption tail develops around 4 eV in yttria stabilized cubic zirconia, which has been attributed to extrinsic absorption[98] or to oxygen vacancy centers in the gap.[99] Moreover, UV-visible diffuse reflectance spectra[100] show a large absorbance below 5.4 eV down to 3.5 eV in pure tetragonal and monoclinic zirconia, an energy range that has not been investigated in Ref. 97. We therefore explore the question of the origin of the electronic excitations seen at low energy in EELS experiment.

To this end, EELS experiments have been performed on the pure monoclinic and tetragonal phases (this will be discussed in detail in Sec. V). For the monoclinic phase, we have been able to fit the low energy part (between 4 and 5 eV) of the spectrum with a $a+b(\varepsilon-E_{\mathrm{gap}})^{3/2}$ law, valid for an indirect gap.[101] Our fitted value for E_{gap} is 3.8 eV in m-ZrO_2 (Table III). For the tetragonal phase, the nanocrystallinity of the sample introduces a high density of grain boundaries, and we find an extrinsic edge around 1.8 eV. For both phases, furthermore, we have been able to fit the energy range between 5 and 7 eV of the spectrum with a $a+b(\varepsilon-E_{\mathrm{gap}})^{1/2}$ law, valid for a direct gap.[101] Our fitted values for E_{gap} are 5.3 for m-ZrO_2 and 5.0 eV for t-ZrO_2, as reported in Table III.

We have also calculated the minimum and direct LDA band gap energy at the theoretical lattice parameters (Table III). Within the accuracy of our calculations, the values of the direct and indirect gaps are within 0.1 eV of each other in all phases except the cubic one, where the minimum gap is 0.5 eV smaller than the first direct gap. Our results agree well with a previous calculation (Kralik *et al.*[13]) performed at the experimental lattice parameters, with the exception of the monoclinic phase. We have also calculated the gaps at the experimental lattice parameters and report these values in Table IV. We find that for the monoclinic phase, the LDA band gap is 0.5 eV larger than that found in Ref. 13.

If the experimental gap observed in EELS at 3.8 eV in m-ZrO_2 turns out to be the fundamental gap, several consequences follow, which we now examine in detail. First, our theoretical and experimental gap values would be in fortuitous agreement with each other in the monoclinic phase, and smaller by 25% with respect to previous EELS experiments performed at a larger momentum transfer.[45,46] The LDA error would therefore be much smaller in ZrO_2 than the usual error found in covalent semiconductors. This rarely occurs, but is

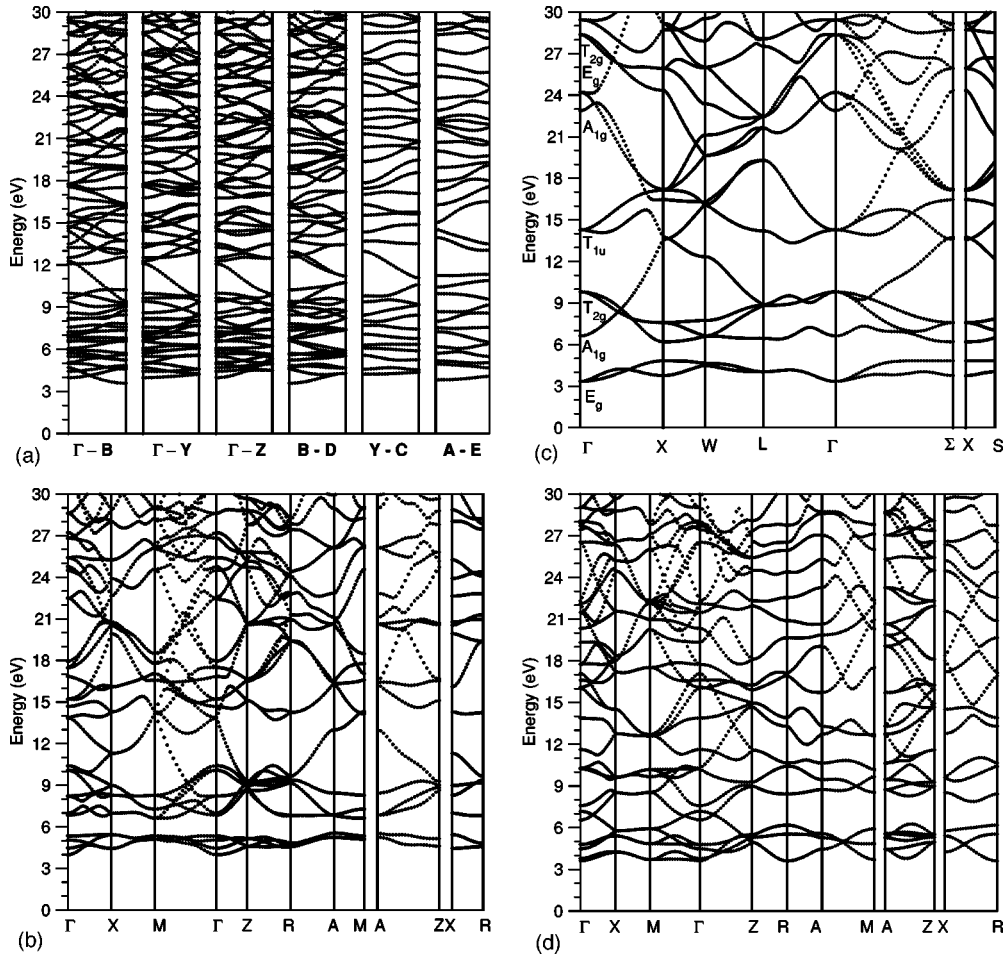

FIG. 6. Theoretical conduction band structure at the equilibrium cell parameters for monoclinic (a), tetragonal (b), cubic (c), and rutile (d) zirconia.

nonetheless plausible, as a comparably small LDA error is found, for example, in α-Al_2O_3.[102,103]

Second, evaluation of the gap value beyond the LDA has been performed: within the standard GW approximation, one expects an approximated quasiparticle shift of around 2.2 eV (Ref. 13) (GW results in Table III). Our LDA gap plus the GW shift leads to a quasiparticle gap of 5.8 eV in m-ZrO_2. Excitonic effects would have to be very large (−2 eV) to compensate for the discrepancy with our EELS experiment.[38] To our knowledge, the excitonic effects that have been reported[98] in zirconia are not as large, and the small electronic dielectric constant ($\varepsilon_\infty \sim 5$) (Ref. 1) makes this improbable.

Third, our LDA calculations also predict a 0.1 eV difference between the onsets of the direct and indirect gap, which is difficult to reconcile with experiment: experimentally, we observe a difference of 1.5 eV between the low energy (indirect) and the high energy (direct) gaps in monoclinic ZrO_2 (Table III). We have checked that the discrepancy cannot be explained theoretically by forbidden transitions at low energy. Indeed, in the cubic phase, first electronic transitions are expected from the top of the valence band (T_{1u} at the Γ point) to the first empty states (E_g at the Γ point), as can be seen from Figs. 4(c) and 6(c). At an energy 2 eV higher, the final states of the transitions are the $A_{1g}+T_{2g}$ states (at the Γ point). We have inspected the optical selection rules in the cubic phase:[54] optical transitions from the T_{1u} to the E_g bands are not forbidden, either at Γ or at the X point (as can also be observed in our absorption spectrum of Fig. 8, center panel).

We would therefore be inclined to conclude that, in our particular case, the fitting of the low energy edge of the EELS spectrum[101] does not allow us to determine the fundamental band gap, at variance with results reported for other materials like GaN.[104] VUV and EELS experiments on m-ZrO_2 can be reconciled if the low energy part of the EELS spectrum is attributed to electronic excitations from defect states, at 2 eV above the top of the intrinsic valence band. They are observed in XPS [Fig. 5(b) and Sec. IV D]. Moreover, positions in the gap of defects in monoclinic zirconia have been calculated:[29] an apparent gap from intersitial oxygen states (3.6 eV) or oxygen vacancy states (3.7 eV) would correspond well to our EELS gap of 3.8 eV. We point out that however these defects should be present in bulk zirconia, and are not caused by irradiation, as we found no evidence of a degradation of our samples in the electron beam.

Last, our value of the fundamental gap in m-ZrO_2 deduced from the fitting of the high energy part of the EELS spectrum is 5.3 eV, in agreement with experiments on thin films[97] and smaller by 0.5 eV with respect to the VUV result

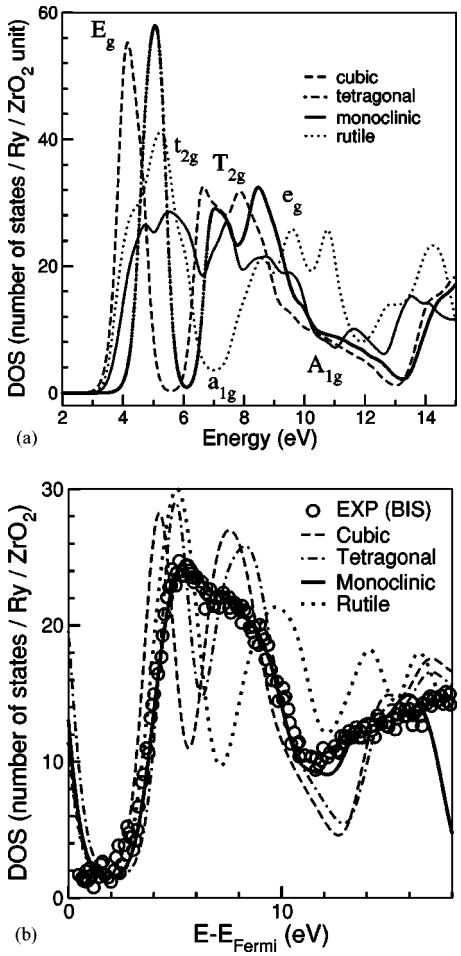

FIG. 7. (a) Density of the early conduction states in the cubic, tetragonal, monoclinic, and rutile phases, and (b) its convolution with a Voigt profile consisting, respectively, of a Gaussian function (half-width at half-maximum of 0.5 eV) and of a Lorentzian function (HWHM of 0.2 eV), compared with experimental Bremsstrahlung isochromat spectrum (Ref. 92) (arbitrary units). Upper (respectively, lower) case labels are the symmetry characters of the DOS of the cubic phase (respectively rutile phase).

deduced from the low absorption edge[88] (Table III). Such an error is reasonable, given the arbitrary nature of the choice of the energy range on which the fit can be performed in both experiments.

We believe that our findings call for new optical and VUV experiments both in m-ZrO_2, in order to, for example, rule out the possibility of a 7.1 eV gap, and also to better identify the interband transition seen at 5.2 eV in thin films, and in pure tetragonal ZrO_2: to our knowledge, no data are available for this phase.

F. Conclusion

In conclusion to this study of the electronic structure of c-, t-, m-, and hypothetical r-zirconia we can therefore make the following points. First, there is a fingerprint in the electronic structure, being the presence of a gap in the conduction band between the E_g and T_{2g} states in the cubic and tetragonal phases, which vanishes in the monoclinic phase

TABLE III. Minimum and direct band gap energy (eV) for the cubic, monoclinic, rutile, and tetragonal phases of ZrO_2, and their location in the Brillouin zone.

Phase			Minimum gaps		Direct gaps
c	This work[b]	$X\rightarrow\Gamma$	3.3	X	3.8
				Γ	3.9
	LDA[a]	$X\rightarrow\Gamma$	3.3		3.7
	GW[a]		5.6		5.8
m	This work[b]	$\Gamma\rightarrow B$	3.6	B	3.7
				Γ	4.0
	LDA[a]	$P_{\Gamma\text{-}X}\rightarrow\Gamma$	3.1	Γ	3.2
	GW[a]		5.4		5.5
Expt.	E_{gap}[c]		3.8		5.3
	EELS[d]		4.2		
	Expt.[e]		4.5		
	VUV[f]				4.5
	VUV[g]				5.8–7.1
	VUV[h]				5.2 and 5.8
r	This work[b]	$\Gamma\rightarrow R$	3.6	Γ	3.6
t	This work[b]	$A\rightarrow\Gamma$	4.0	Γ	4.1
		$P_{\Gamma\text{-}M}\rightarrow\Gamma$	4.0		
		$P_{\Gamma\text{-}X}\rightarrow\Gamma$	4.0		
		$Z\rightarrow\Gamma$	4.0		
	LDA[a]	$P_{\Gamma\text{-}M}\rightarrow\Gamma$	4.1	Γ	4.3
	GW[a]		6.4		6.6
Expt.	E_{gap}[c]				5.0

[a]Theory at the experimental lattice parameters (Ref. 13).
[b]At the theoretical equilibrium lattice parameters.
[c]This work, fit of EELS experiment, see text.
[d]Reference 45.
[e]EELS (Ref. 46), and REELS (Ref. 95).
[f]Reference 96.
[g]Reference 88.
[h]On thin films, Ref. 97.

because of the partially octahedral crystal field. This can help in discriminating the monoclinic phase from the other phases.

Second, we find that the electronic structure of the cubic and tetragonal phases are similar. The main difference comes from a sharper valence band edge in tetragonal zirconia and a redshift of the Zr 4*s*, 4*p* and O 2*s* lines in the cubic spectrum with respect to the tetragonal phase.

Third, the 8 eV width of the O 2*s* band in the XPS experiment[88] is left unexplained by LDA or quasiparticle calculations. This particular point could be elucidated with the aid of new experiments.

Finally, we note that in the EELS experiment, we confirm a low energy gap of zirconia around 4 eV that we attribute to defect states, and find a high energy gap at 5.3 eV in m-ZrO_2, close to the 5.2 or 5.8 eV observed in VUV experiments. This would lead us to conclude that for this particular material, the fitting of the low energy edge of the EELS spectrum is not appropriate to determine the fundamental gap. A new optical determination of the fundamental gap in

TABLE IV. Minimum and direct calculated band gap energy (eV) for the cubic, monoclinic, and tetragonal phases of ZrO_2 at theoretical and experimental lattice parameters (LP). $P_{\Gamma\text{-}M}$ is found at 0.6 (respectively, 0.55) $|\Gamma\text{-}M|$ for the theoretical (respectively, experimental) (LP). $P_{\Gamma\text{-}X}$ is found at 0.63 (respectively, 0.65) $|\Gamma\text{-}X|$ for the theoretical (respectively, experimental) LP.

Phases	Gaps	Theor. LP	Expt. LP
c	$X\rightarrow\Gamma$	3.34	3.25
	X	3.76	3.65
	Γ	3.90	3.80
m	$\Gamma\rightarrow B$	3.58	3.59(4)
	B	3.66	3.59(2)
	Γ	3.98	3.93
t	$A\rightarrow\Gamma$	3.99	4.23
	$P_{\Gamma\text{-}M}\rightarrow\Gamma$	4.00	4.03
	$P_{\Gamma\text{-}X}\rightarrow\Gamma$	4.01	4.08
	$Z\rightarrow\Gamma$	4.02	4.15
	Γ	4.11	4.20

both pure monoclinic and tetragonal zirconia would be worthwhile.

V. ELECTRON ENERGY-LOSS SPECTROSCOPY

In this section, we first apply the theoretical framework defined in Sec. II and report our theoretical EELS spectra (Sec. V A). Valence EELS experiments have previously been performed in transmission at large momentum transfer q (Refs. 45 and 46) and in reflection.[48] In this work, we have performed very low q experiments (Sec. V B) and compare them to the theoretical results (Sec. V C). In previous work,[40,43,105,106] we have shown that local-field effects can be the main source of anisotropy in the response function: in the RPA without local fields, the response function shows only weak anisotropy, reflecting the quasi-isotropy of the coupling of the radiation to the band structure, whereas including local-field effects causes anisotropies visible in the EELS spectrum (for example, excitation of 3*p* plasmons in rutile[40]), or cause the static birefringence of superlattices.[105,106] Here, we will show that the theoretical 4*p* plasmons in the EELS evolve in the different crystalline phases of zirconia through local-field effects.

A. Theoretical EELS spectrum

In Fig. 8, we report the dielectric function ε for *c*-ZrO_2 calculated in the RPA without local fields: the real part ε_1 is shown in the top panel, the imaginary part ε_2 (corresponding to the absorption spectrum) in the center panel, and in the bottom panel we show the loss function, defined as $-\mathrm{Im}(\varepsilon^{-1})$, which in this approximation is equal to $\varepsilon_2/(\varepsilon_1^2+\varepsilon_2^2)$. Three regions can be distinguished. First, we observe that the valence excitation region extends up to 18.5 eV. The real part of ε behaves mainly as a double (classical) oscillator.[107] It vanishes (from positive to negative value) around 8.8 and 16.5 eV, and, correspondingly, ε_2 shows

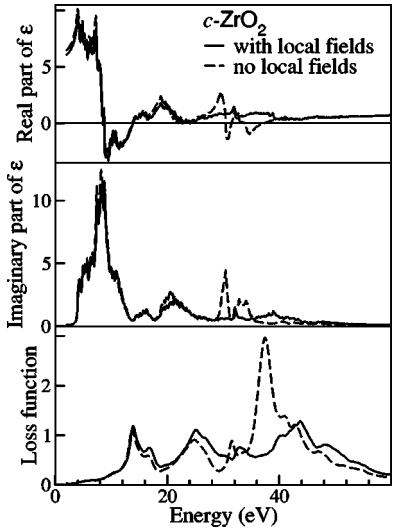

FIG. 8. Theoretical dielectric function for *c*-ZrO_2. Top panel, real part. Center panel, imaginary part. Bottom panel, the loss function. Solid lines, RPA with local fields. Dashed lines, without local fields. The real and imaginary parts of the dielectric function (respectively, the loss function) are broadened with a Lorentzian of HWHM of 0.1 eV (respectively, 0.5 eV).

maxima of absorption at these frequencies. The real part ε_1 vanishes (from negative to positive) at 13.7 and at 16.5 eV (not seen in the figure because of the small broadening). The loss function consequently shows two peaks at these energies. In the absorption spectrum ε_2, the strong absorption below 9.5 eV stems from transitions from the valence band to the E_g states. The absorption band extending beyond 9.5 up to 16 eV is associated with transitions from the valence band to T_{2g} states in the conduction band. The small absorption peak at 16 eV comes from valence band to A_{1g} excitations.

Second, we see that at above 28 eV, corresponding to the zirconium 4*p* excitations, ε_1 also behaves as a triple classical oscillator: it vanishes (from positive to negative) at 30.4, 32.8, and 34.0 eV. Consequently ε_2 shows strong absorption at 30.5 eV and between 32.9 and 34.1 eV. Peaks are observed in the loss function when ε_1 vanishes (from negative to positive) at 31.5, 33.4, and 37.7 eV.

Third, we remark that the region between the valence plasmons and the 4*p* plasmons, i.e., around 16 to 28 eV, cannot be interpreted in terms of classical oscillators. Between 22 and 28 eV, ε_1 and ε_2 are dominated by linear features, increasing for ε_1 and decreasing for ε_2. The corresponding loss function exhibits a broadened peak at 24.9 eV which we assign *not* to plasmons but to other forms of collective excitations. The plasmon is defined by a vanishing real part of the dielectric function and a minimum of the imaginary part, which is not the case for this peak. Such linear behavior for ε_1 and ε_2 has already been observed in the theoretical EELS of rutile TiO_2.[40] However, we note that here the oscillators associated with the O 2*s* electrons are present (ε_1 vanishes from positive to negative around 20.0 eV, and vanishes from negative to positive around 24.7 eV) but are overwhelmed by the linear behavior of ε_1 and ε_2, which is the cause of the main peak at 24.9 eV.

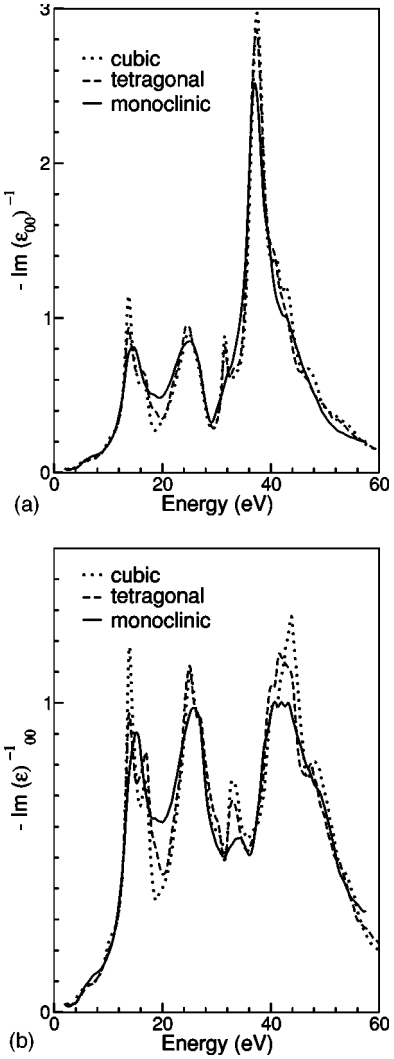

FIG. 9. Theoretical loss function (a) within the RPA without local fields, and (b) with local-field effects. Dotted line, c-ZrO_2. Dashed line, t-ZrO_2. Solid line, m-ZrO_2. The loss function is broadened with a Lorentzian of HWHM of 0.5 eV.

The local-field effects reflect the inhomogeneity of the material in the response function, and have the effect of mixing the formerly independent transitions, as shown in the solid lines of Fig. 8. The effects on ε_1 and ε_2 are weak below 25 eV. At higher energies, however, they drastically modify the triple 4p plasmons, both in line shape and peak position. The peak formerly at 31.5 eV is shifted towards higher energy by 1.4 eV, while the main peak is shifted by 6.4 eV. Large effects on excitations from a quasiatomic level due to local fields have already been found for the 3p excitations in rutile TiO_2.[40]

Having examined the loss function of the cubic phase in detail, we now look at the other phases. The loss function for c-, t-, and m-ZrO_2 is reported, without local-field effects, in Fig. 9(a). We find a small anisotropy for the tetragonal and monoclinic phases. The spectra reported in Figs. 9(a) and 9(b) are averaged over momentum transfer along the three Cartesian axes. When averaged, the 4p peak at 31.5 eV is smeared out in the spectrum of the monoclinic phase, but is nonetheless visible in the tetragonal phase. The main 4p peak around 37 eV is very similar in the three phases, showing a very weak dependence of this excitation on the crystalline phase in the RPA without local fields.

When local-field effects are included in the calculations [Fig. 9(b)], the modification of the main 4p plasmons strongly depends on the crystalline phase: the main peak is shifted by 6.4 eV in c-ZrO_2, by 4.2 eV in t-ZrO_2, and becomes a triplet shifted by 3.8, 5.0, and 6.3 eV in the monoclinic phase. Additionally, we note that the shape of peak formerly at 31.5 eV varies. The dependence of the 4p plasmon on the crystalline phase is therefore brought into the spectrum through local-field effects.

B. Experimental details

Monoclinic ZrO_2 reference spectra were recorded from thin foils prepared from bulk samples. The bulk samples were obtained by sintering of undoped powders commercialized by the Tosoh Japanese company under the name TZ-0 (purity, 99.9% ZrO_2; particle size, 40 to 60 nm). Tetragonal and cubic ZrO_2 reference spectra were recorded from homemade powders dispersed on a copper grid covered with a perforated carbon thin film. Both were synthesized by the spray-pyrolysis technique.[108] One advantage of this procedure is to obtain nanocrystallized powders and to keep the tetragonal structure stable at room temperature without the use of dopants. The cubic structure was stabilized by addition of 8.5 mol% Y_2O_3.

The EELS analyses were performed using a TECNAI F20 Supertwin microscope fitted with a Gatan Image Filter. With this setup, the probe is very small and our energy resolution is better than 0.7 eV. The spectra were recorded in scanning transmission electron microscopy mode with an energy dispersion of 0.1 eV/channel, using low collection angles (1.8 to 0.5 mrad) to increase the resolution and reduce as much as possible the momentum transfers, while keeping an optimum signal to noise ratio. The spectra were then processed using the Electronic Structure Tools software (EST)[109] to calculate the single scattering spectra. The removal of the zero-loss peak and plural scattering signal are based on a Fourier-log deconvolution after fitting of the experimental zero-loss peak with a Pearson VII function.

C. Comparison with experimental EELS spectrum

In our calculations, we have used a vanishing momentum transfer ($q=0$). In our experiments, we estimate the transferred momentum to be 0.12 $Å^{-1}$ in t zirconia, and to amount to 0.45 $Å^{-1}$ in m- and YS c-ZrO_2. Calculations performed in the cubic phase at vanishing q or at $q=0.2$ $Å^{-1}$ did not show any difference in peak positions in the loss function, and only a tiny difference (at most 7%) in peak intensities: this enables us to compare directly our experimental and theoretical spectra for the tetragonal phase, and gives us confidence in the comparison of the theoretical and experimental spectra in the monoclinic and cubic phases.

In the experiment, the observed intensity depends on an integration of the signal over the collection angle β,[110] which for a cubic phase is expressed by the formula

$$I(E) \propto -\pi \,\mathrm{Im}\left[\varepsilon^{-1} \ln\left(1+\frac{\beta^2}{\theta_E^2}\right)\right], \tag{6}$$

where $\theta_E = E_{\mathrm{loss}} m/\hbar^2 k_0^2$ is the characteristic angle depending on the energy loss E_{loss}, and on the relativistic mass m and wave vector k_0 of the incident electron beam.

For the tetragonal phase, we have averaged the integration over the geometries in which the momentum transfer is parallel or perpendicular to the tetragonal c axis,

$$I(E) = \frac{I^{q\|c}(E) + 2I^{q\perp c}(E)}{3}. \tag{7}$$

We find that the intensity when q is along the tetragonal axis is given by

$$I^{q\|c}(E) \propto -\pi \,\mathrm{Im}\left[\varepsilon_\perp^{-1} \ln\left(1+\frac{\beta^2\varepsilon_\perp}{\theta_E^2\varepsilon_\|}\right)\right]. \tag{8}$$

When q is parallel to the tetragonal axis, we must furthermore integrate taking into account the in-plane component of the q vector defined by the in-plane angle ϕ,

$$I^{q\perp c}(E) \propto -\pi \,\mathrm{Im}\left[\int_0^{2\pi} \frac{1}{\theta(\phi)} \ln\left(1+\frac{\beta^2\theta(\phi)}{\theta_E^2\varepsilon_\|}\right) d\phi\right], \tag{9}$$

$$\theta(\phi) = \varepsilon_{\perp,[100]} \cos^2\phi + \varepsilon_{\perp,[010]} \sin^2\phi. \tag{10}$$

For the monoclinic phase, we have averaged the integrated intensity for q along the three crystal directions calculated with Eq. (9). For q along the [001] direction perpendicular to the basal plane, the integrated intensity is again given by Eqs. (9) and (10). When q is along [100] (respectively [010]), Eq. (10) is an approximation to the integration, and so we have

$$\theta(\phi) \approx \varepsilon_{\perp,[010]} \cos^2\phi + \varepsilon_{\perp,[001]} \sin^2\phi. \tag{11}$$

To compare our theoretical spectra to the experimental ones, we have applied integrations of Eqs. (6)–(11) of our theoretical dielectric functions with $\beta = 1.8$ mrad for the cubic and monoclinic phases, and $\beta = 0.5$ mrad for the tetragonal phase.

The experimental and peak positions of the integrated loss function are reported in Table V. Compared to peak positions of the loss functions reported in Fig. 9, the integration over β affects the position of the collective excitation by at most 0.3 eV, the valence plasmon position by 1.0 (t), 0.6 (m), and 0.5 (c) eV, and the $4p$ plasmon main peak by −0.6 (c), 0.3 (t), and −0.2 (m) eV.

We have seen that, in contrast to the plasmon peaks, the collective excitation does not depend precisely on the frequency at which the real part of the dielectric function vanishes. We find its theoretical position in very good agreement with experiment for all the crystalline phases, as also already seen in a previous work[40] (Table V). We have therefore used this as our reference: we have fitted the broadening of our theoretical integrated loss functions in the monoclinic phase to the experiment, and applied the resulting Voigt profile to the spectra of the tetragonal and cubic phases.

TABLE V. Experimental position (eV) of the plasmons and of the collective excitation in c-, t-, and m-ZrO_2. In the experiment, c-ZrO_2 is yttria stabilized. The theoretical values (RPA with local fields) are given in parentheses. In the calculations, the valence plasmon has two peaks in c- and t-ZrO_2.

Phase	Valence plasmons		Collective excitation		$4p$ plasmons	
c	14.4	(14.5)	24.8	(25.4)		(33.2)
		(16.8)			41.5	(43.2)
t	14.4	(14.9)	25.4	(25.2)		(32.9)
		(17.0)			42.3	(41.9)
m	14.4	(15.9)	25.8	(25.4)		(33.9)
					41.2	(41.8)

The theoretical and experimental integrated loss function of pure monoclinic and tetragonal zirconia are reported in Figs. 10(a) and 10(b), respectively. The main $4p$ plasmon agrees well, both in position and shape, for the two phases, provided that local-field effects are included (see insets of Fig. 10 for the result without local-field effects). A RPA with local-field effects scheme therefore seems reasonable for this type of excitation. This might come from a partial cancellation of further many-body effects, treating the electron-electron and the electron-hole interaction.[38] In contrast, the theoretical position of the valence plasmon is too high in energy by 1.5 eV in m-ZrO_2, and by 0.5 eV in t-ZrO_2. In both phases the theoretical intensity of the valence plasmon is too small, and the shape of the low-loss part is not well reproduced. In that case, inclusion of many-body effects, in particular excitonic effects, in the theoretical spectra would be helpful. However, one must be cautious in the interpretation of the intensity of the low energy plasmon, as a precise determination of the experimental intensity in the low energy part of the loss spectrum can be very sensitive to the subtraction of the zero-loss peak.

Finally, in Fig. 10(c), we compare pure zirconia (theory) with yttria-stabilized zirconia (experiment). We find that the introduction of yttria affects the whole electron energy loss spectrum: the valence plasmon position now (fortuitously) agrees, although the theoretical intensity is underestimated. The impact of the yttria concentration on the valence plasmon has been previously reported.[48] We note also that the width of the collective excitation is larger in the experiment, and that the main $4p$ plasmon peak is redshifted by more than 1 eV in the experimental result with respect to the calculation for the pure phase.

D. Conclusion

In conclusion to this section, we have found that the theoretical valence plasmon(s) as well as the $4p$ plasmons differ both in peak position and shape in the three low pressure phases of zirconia. These differences have two origins: for the valence plasmon, the difference in the line shape arises directly from differences in the band structure between the phases, like the gap in the conduction states detailed in Sec.

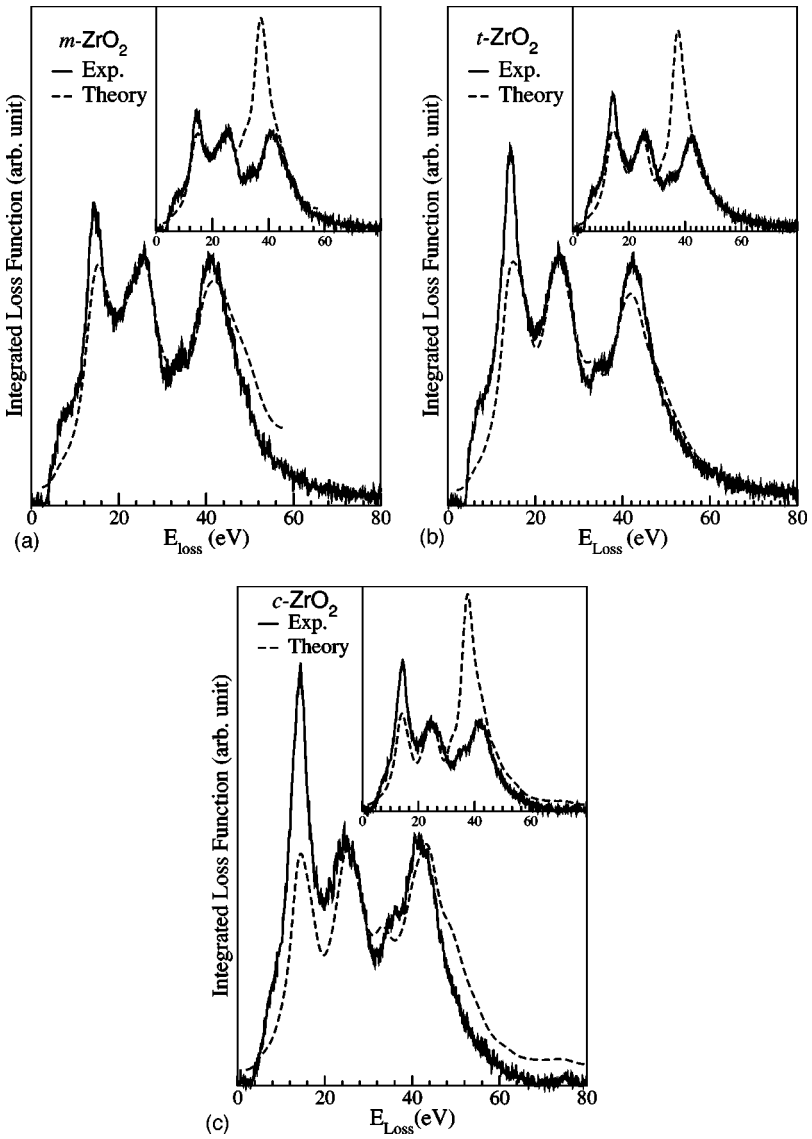

FIG. 10. Integrated loss function (see text) for pure zirconia: (a) monoclinic, (b) tetragonal, and (c) cubic phases. Solid line, experiment. Dashed line, theory with local fields. Inset, theory without local fields. The theoretical curves have been convoluted with a Voigt profile, Gaussian of HWHM of 1 eV, and Lorentzian function of HWHM of 1 eV. In the experiment, cubic zirconia is yttria stabilized.

IV. For the 4*p* peak ($N_{2,3}$ edge), the difference is brought in via the local-field effects. These differences are not observed in the experiment, partly because of the accuracy of the measurements, partly because of the difficulty to synthetize appropriate samples. In this respect, core spectroscopy, such as electron energy-loss near-edge spectroscopy[36,37] seems of greater potential for the characterization and localization of yttria in the structure of zirconia.

VI. CONCLUSION

In conclusion, we have performed an *ab initio* study of the atomic and electronic structures of the three low-pressure (monoclinic, tetragonal, and cubic) phases of zirconia. Within the DFT-LDA framework, we have found it necessary to include the 4*sp* semicore states in the calculations. From comparison of the theoretical bulk modulus with experiments performed in the cubic phase, we have found that introduction of yttria in zirconia lowers the bulk modulus by as much as 30%.

We have then followed the effect on the electronic structure as the crystal field evolves from tetrahedral, as in the cubic and tetragonal structures, to octahedral as in the hypothetical rutile phase, via the intermediate monoclinic phase. We have described a fingerprint in the electronic structure of cubic and tetragonal zirconia: the presence of a gap in the conduction band separating the E_g and $A_{1g}+T_{2g}$ states, which we have shown does not occur in *m*-ZrO_2. The cubic and tetragonal electronic structures are otherwise very similar, except for the presence of a high density of states at the top of the valence band of *t*-ZrO_2, which shifts the Zr 4*s*, Zr 4*p* lines and the O 2*s* band to higher energies. We found otherwise that the LDA error on the peak positions of the Zr 4*p* lines and O 2s band are similar despite the stronger atomic character of the *Zr* 4*p*.

We have performed EELS experiments at small momentum transfer on pure monoclinic and tetragonal zirconia, and on the yttria stabilized cubic phase. In *m*-ZrO_2, we find excitations at around 4 eV which we attribute to defect states. By fitting the high energy part of the spectrum, we find a gap at 5.3 eV in *m*-ZrO_2, close to the 5.2 or 5.8 eV observed in VUV experiment. This would lead us to conclude that for this particular material, the fitting of the low energy edge of

the EELS spectrum is not appropriate to determine the fundamental band gap.

Finally, we have performed calculations of the electron energy-loss spectra of zirconia in the random phase approximation and included local-field effects. Differences between the phases in the electronic structures are reflected in the line shape of the valence plasmons. The differences in the 4*p* plasmons between the phases are caused by the local-field effects.

We thank Thierry Lépicier for fruitful discussions at the early stage of this work, Virginie Quéquet for the SIC calculation on the Zr atom, and Jean-Marc Costantini for having drawn our attention to some of the published experimental work. Ground-state calculations have been performed using the PWSCF package.[49] Calculations of the dielectric properties were performed using the DP code developed at the Laboratoire des Solides Irradiés.[111] Figure 1 was produced using XCrySDen.[112] The work of L.K.D. and Ph.B. was funded by the joint research program "ISMIR" between CEA and CNRS. Computer time has been granted by CEA/DSM on the cluster of Compaq Alphaserver (project p543) and NEC SX6 (project p93) and by IDRIS on the NEC SX5 (project N 544). This work was funded in part by the EU's 6th Framework Programme through the NANOQUANTA Network of Excellence (NMP4-CT-2004-500198).

*Electronic address: louise.dash@polytechnique.fr
†Electronic address: nathalie.vast@polytechnique.fr
‡Present address: Electricité de France, Centre des Renardières, 77818 Moret-sur-Loing, France.

[1] X. Zhao and D. Vanderbilt, Phys. Rev. B **65**, 075105 (2002).
[2] T. Ishikawa, H. Yamaoka, Y. Harada, T. Fujii, and T. Nagasawa, Nature (London) **416**, 64 (2002).
[3] S. Meriani, *Zirconia'88. Advances in Zirconia Science and Technology* (Elsevier, New York, 1989).
[4] E. J. Walter, S. P. Lewis, and A. M. Rappe, Surf. Sci. **95**, 44 (2001).
[5] V. Fiorentini and G. Gulleri, Phys. Rev. Lett. **89**, 266101 (2002).
[6] R. Puthenkovilakam, E. A. Carter, and J. P. Chang, Phys. Rev. B **69**, 155329 (2004).
[7] A. Meldrum, L. A. Boatner, and R. C. Ewing, Phys. Rev. Lett. **88**, 025503 (2002).
[8] C. Morant, J. M. Sanz, and L. Galán, Phys. Rev. B **45**, 1391 (1992).
[9] R. Orlando, C. Pisani, C. Roetti, and E. Stefanovich, Phys. Rev. B **45**, 592 (1992).
[10] S. Gennard, F. Corà, and C. R. A. Catlow, J. Phys. Chem. B **103**, 10 158 (1999).
[11] J. K. Dewhurst and J. E. Lowther, Phys. Rev. B **57**, 741 (1998).
[12] J. E. Lowther, J. K. Dewhurst, J. M. Leger, and J. Haines, Phys. Rev. B **60**, 14 485 (1999).
[13] B. Králik, E. K. Chang, and S. G. Louie, Phys. Rev. B **57**, 7027 (1998).
[14] H. J. F. Jansen, Phys. Rev. B **43**, 7267 (1991).
[15] G. Jomard, T. Petit, A. Pasturel, L. Magaud, G. Kresse, and J. Hafner, Phys. Rev. B **59**, 4044 (1999).
[16] H. J. F. Jansen and J. A. Gardner, Physica B & C **150B**, 10 (1988).
[17] F. Zandiehnadem, R. A. Murray, and W. Y. Ching, Physica B & C **150B**, 19 (1988).
[18] N. I. Medvedeva, V. P. Zhukov, M. Ya. Khodos, and V. A. Gubanov, Phys. Status Solidi B **160**, 517 (1990).
[19] G. M. Rignanese, F. Detraux, X. Gonze, and A. Pasquarello, Phys. Rev. B **64**, 134301 (2001).
[20] S. Fabris, A. T. Paxton, and M. W. Finnis, Phys. Rev. B **63**, 094101 (2001).
[21] G. Fadda, L. Truskinovsky, and G. Zanzotto, Phys. Rev. B **66**, 174107 (2002).
[22] A. P. Mirgorodsky, M. B. Smirnov, and P. E. Quintard, Phys. Rev. B **55**, 19 (1997).
[23] K. Negita and H. Takao, J. Phys. Chem. Solids **50**, 325 (1989).
[24] K. Parlinski, Z-.Q. Li, and Y. Kawazoe, Phys. Rev. Lett. **78**, 4063 (1997).
[25] M. Wilson, U. Schönberger, and M. W. Finnis, J. Phys. Chem. Solids **50**, 325 (1996).
[26] M. W. Finnis, A. T. Paxton, M. Methfessel, and M. van Schilfgaarde, Phys. Rev. Lett. **81**, 5149 (1998).
[27] E. V. Stefanovich, A. L. Shluger, and C. R.A. Catlow, Phys. Rev. B **49**, 11 560 (1994). See Refs. 67, 73, and 77 herein.
[28] G. Stapper, M. Bernasconi, N. Nicoloso, and M. Parrinello, Phys. Rev. B **59**, 797 (1999). For the monoclinic phase, the b/a was probably misprinted. We have calculated the monoclinic b parameter from the volume and the other cell parameters.
[29] A. S. Foster, V. B. Sulimov, F. Lopez Gejo, A. L. Shluger, and R. M. Nieminen, Phys. Rev. B **64**, 224108 (2001).
[30] S. Ostanin, E. Salamatov, A. J. Craven, D. W. McComb, and D. Vlachos, Phys. Rev. B **66**, 132105 (2002).
[31] A. Bogicevic and C. Wolverton, Phys. Rev. B **67**, 024106 (2003).
[32] A. Eichler, Phys. Rev. B **64**, 174103 (2001).
[33] D. A. Müller, D. J. Singh, and J. Silcox, Phys. Rev. B **57**, 8181 (1998).
[34] S. Nufer, A. G. Marinopoulos, T. Gemming, C. Elsässer, W. Kurtz, S. Köstlmeier, and M. Rühle, Phys. Rev. Lett. **86**, 5066 (2001).
[35] D. A. Pankhurst, G. A. Botton, and C. J. Humphreys, Phys. Rev. B **63**, 205117 (2001).
[36] I. M. Ross, W. M. Rainforth, A. J. Scott, A. P. Brown, R. Brydson, and D. W. McComb, Inst. Phys. Conf. Ser. **168**, 303 (2001).
[37] S. Ostanin, A. J. Craven, D. W. McComb, D. Vlachos, A. Alavi, A. T. Paxton, and M. W. Finnis, Phys. Rev. B **65**, 224109 (2002).
[38] G. Onida, L. Reining, and A. Rubio, Rev. Mod. Phys. **74**, 601 (2002).
[39] A. Marini, R. Del Sole, and A. Rubio, Phys. Rev. Lett. **91**, 256402 (2003).
[40] N. Vast, L. Reining, V. Olevano, P. Schattschneider, and B. Jouffrey, Phys. Rev. Lett. **88**, 037601 (2002).
[41] V. Olevano and L. Reining, Phys. Rev. Lett. **86**, 5962 (2001).
[42] A. G. Marinopoulos, L. Reining, V. Olevano, A. Rubio, T. Pichler, X. Liu, M. Knupfer, and J. Fink, Phys. Rev. Lett. **89**, 076402 (2002).
[43] A. G. Marinopoulos, L. Reining, A. Rubio, and N. Vast, Phys.

Rev. Lett. **91**, 046402 (2003).
[44] A. Marini, R. Del Sole, and G. Onida, Phys. Rev. B **66**, 115101 (2002).
[45] D. W. McComb, Phys. Rev. B **54**, 7094 (1996).
[46] J. Frandon, B. Brouseau, and F. Pradal, Phys. Status Solidi B **98**, 379 (1980).
[47] F. Yubero, J. M. Sanz, J. F. Trigo, E. Elizalde, and S. Toogard, Surf. Interface Anal. **22**, 124 (1994).
[48] F. Yubero, J. P. Espinós, and A. R. Gonzáles-Elipe, J. Vac. Sci. Technol. A **16**, 2287 (1998).
[49] S. Baroni *et al.*, http://www.pwscf.org
[50] S. Baroni, S. de Gironcoli, A. Dal Corso, and P. Giannozzi, Rev. Mod. Phys. **73**, 515 (2001).
[51] G. B. Bachelet, D. R. Hamann, and M. Schlüter, Phys. Rev. B **26**, 4199 (1982).
[52] H. J. Monkhorst and J. D. Pack, Phys. Rev. B **13**, 5188 (1976).
[53] C. J. Bradley and A. P. Cracknell, *The Mathematical Theory of Symmetry in Solids* (Clarendon, Oxford, 1972).
[54] F. Bassani and G. P. Parravicini, *Electronic States and Optical Transitions in Solids* (Pergamon, Oxford, 1975).
[55] H. Ehrenreich and M. H. Cohen, Phys. Rev. **155**, 786 (1959).
[56] S. L. Adler, Phys. Rev. **126**, 413 (1962).
[57] N. Wiser, Phys. Rev. **129**, 62 (1963).
[58] E. Runge and E. K. U. Gross, Phys. Rev. Lett. **52**, 997 (1984).
[59] E. K. U. Gross and W. Kohn, Phys. Rev. Lett. **55**, 2850 (1985).
[60] F. Aryasetiawan, O. Gunnarsson, M. Knupfer, and J. Fink, Phys. Rev. B **50**, 7311 (1994).
[61] R. J. Ackermann, S. P. Garg, and E. G. Rauh, J. Am. Ceram. Soc. **60**, 341 (1977).
[62] *Phase Equilibria Diagrams*, edited by A. E. McHale and R. S. Roth (National Institute of Standards and Technology, Gaithersburg, MD, 1996).
[63] O. Ohtaka, T. Yamanaka, and S. Kume, J. Am. Ceram. Soc. **74**, 2321 (1991).
[64] C. J. Howard, E. H. Kisi, and O. Ohtaka, J. Am. Ceram. Soc. **74**, 505 (1991).
[65] O. Ohtaka, H. Fukui, T. Kunisada, T. Fujisawa, K. Funakoshi, W. Utsumi, T. Irifune, K. Kuroda, and T. Kikegawa, Phys. Rev. B **63**, 174108 (2001).
[66] S. Desgreniers and K. Lagarec, Phys. Rev. B **59**, 8467 (1999).
[67] R. J. Ackermann, E. G. Rauh, and C. A. Alexander, High. Temp. Sci. **7**, 305 (1975).
[68] D. K. Smith and H. W. Newkirk, Acta Crystallogr. **18**, 983 (1965).
[69] G. Teufer, Acta Crystallogr. **15**, 1187 (1962).
[70] H. Boysen, F. Frey, and T. Vogt, Acta Crystallogr., Sect. B: Struct. Sci. **47**, 881 (1991).
[71] F. Frey, H. Boysen, and T. Vogt, Acta Crystallogr., Sect. B: Struct. Sci. **46**, 724 (1990).
[72] D. Simeone, G. Baldinozzi, D. Gosset, M. Dutheil, A. Bulou, and T. Hansen, Phys. Rev. B **67**, 064111 (2003).
[73] P. Aldebert and J. P. Traverse, J. Am. Ceram. Soc. **68**, 34 (1985).
[74] M. Jouanne, J. F. Morhange, M. A. Kanehisa, E. Haro-Poniatowski, G. A. Fuentes, E. Torres, and E. Hernàndez-Tellez, Phys. Rev. B **64**, 155404 (2001).
[75] D. N. Argyriou, M. M. Elcombe, and A. Larson, J. Phys. Chem. Solids **57**, 183 (1996).
[76] A. Feinberg and C. H. Perry, J. Phys. Chem. Solids **42**, 513 (1981).
[77] C. J. Howard, R. J. Hill, and B. E. Reichert, Acta Crystallogr., Sect. B: Struct. Sci. **B44**, 116 (1988).
[78] H. M. Kandil, J. D. Greinerand, and J. F. Smith, J. Am. Ceram. Soc. **67**, 341 (1984).
[79] R. P. Ingel and D. Lewis, J. Am. Ceram. Soc. **71**, 265 (1988).
[80] M. Fukuhara and I. Yamauchi, J. Mater. Sci. **28**, 4681 (1993).
[81] M. V. Nevitt, S.-K. Chan, J. Z. Liu, M. H. Grimsditch, and Y. Fang, Physica B & C **150B**, 230 (1988).
[82] J. M. Leger, P. E. Tomaszewski, A. Atouf, and A. S. Pereira, Phys. Rev. B **47**, 14 075 (1993).
[83] A. Christensen and E. A. Carter, Phys. Rev. B **58**, 8050 (1998).
[84] S. G. Louie, S. Froyen, and M. L. Cohen, Phys. Rev. B **26**, 1738 (1982).
[85] F. D. Murnaghan, Proc. Natl. Acad. Sci. U.S.A. **30**, 244 (1944).
[86] R. Hill, Proc. Phys. Soc., London, Sect. A **65**, 349 (1952).
[87] R. P. Ingel and D. Lewis, J. Am. Ceram. Soc. **69**, 325 (1986).
[88] R. H. French, S. J. Glass, F. S. Ohuchi, Y. N. Xu, and W. Y. Ching, Phys. Rev. B **49**, 5133 (1994).
[89] J. P. Perdew and A. Zunger, Phys. Rev. B **23**, 5048 (1981).
[90] A. Svane and O. Gunnarsson, Phys. Rev. B **37**, 9919 (1988).
[91] A. Svane and O. Gunnarsson, Phys. Rev. Lett. **65**, 1148 (1990).
[92] L. Soriano, M. Abbate, J. Faber, C. Morant, and J. M. Sanz, Solid State Commun. **93**, 659 (1995).
[93] From the integration of the projected DOS in this energy range, 84% of the charge comes from the oxygen 2*s* electronic states.
[94] F. Himpsel (private communication).
[95] E. Elizalde, J. M. Sanz, F. Yubero, and L. Galan, Surf. Interface Anal. **16**, 213 (1990).
[96] R. S. Sokolova, Sov. J. Appl. Phys. **41**, 454 (1974).
[97] C.-K. Kwok and C. R. Aita, J. Appl. Phys. **66**, 2756 (1989).
[98] P. Camagni, P. Galinetto, G. Samoggia, and N. Zema, Solid State Commun. **83**, 943 (1992).
[99] V. M. Orera, R. I. Merino, Y. Chen, R. Cases, and P. J. Alonso, Phys. Rev. B **42**, 9782 (1990).
[100] M. Li, Z. Feng, G. Xiong, P. Ying, Q. Xin, and C. Li, J. Phys. Chem. **105**, 8107 (2001).
[101] B. Rafferty and L. M. Brown, Phys. Rev. B **58**, 10326 (1998).
[102] A. G. Marinopoulos and C. Elsässer, Acta Mater. **48**, 4375 (2000).
[103] E. Gaudry, Ph.D. thesis,University Paris 6, 2004.
[104] S. Lazar, G. A. Botton, M.-Y. Wu, F. D. Tichelaar, and H. W. Zandbergen, Ultramicroscopy **96**, 535 (2003).
[105] S. Botti, N. Vast, L. Reining, V. Olevano, and L. C. Andreani, Phys. Rev. Lett. **89**, 216803 (2003).
[106] S. Botti, N. Vast, L. Reining, V. Olevano, and L. Andreani, Phys. Rev. B **70**, 045301 (2004).
[107] J. T. Houghton and S. D. Smith, *Infra-red Physics* (Clarendon, Oxford, 1966).
[108] E. Djurado and J. Meunier, J. Solid State Chem. **141**, 191 (1998).
[109] L. DeNoyer and G. Duscher, Electronic Structure Tool (EST) software, Tompkins County Trust Company Inc., Ithaca, NY, developed under Gram 32, Galactic Industries, 1996, Gram/32 325, Salem, NH.
[110] R. F. Egerton, *Electron Energy-Loss Spectroscopy in the Microscope* (Plenum, New York, 1986).
[111] V. Olevano *et al.*, http://theory.lsi.polytechnique.fr/codes/dp/
[112] A. Kokalj, J. Mol. Graphics Modell. **17**, 176 (1999). Code available from http://www.xcrysden.org/